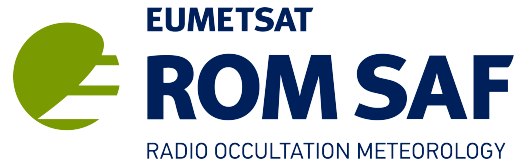


ROM SAF Report 33  
Ref: SAF/ROM/METO/REP/RSR/033  
Web: [www.romsaf.org](http://www.romsaf.org)  
Date: 14 September 2018



## **ROM SAF Report 33**

Some science changes in ROPP-9.1

S. B. Healy

ECMWF, Reading, UK

### Document Author Table

	<i>Name</i>	<i>Function</i>	<i>Date</i>	<i>Comments</i>
<b>Prepared by:</b>	S. B. Healy	ROM SAF Project Team	14 September 2018	
<b>Reviewed by:</b>	I. D. Culverwell	ROM SAF review	30 May 2018	
<b>Approved by:</b>	K. B. Lauritsen	ROM SAF Project Manager	2 July 2018	

### Document Change Record

<i>Issue/Revision</i>	<i>Date</i>	<i>By</i>	<i>Description</i>
0.1	22 May 2018	SBH	1st draft
0.2	8 June 2018	SBH	2nd draft after reviewer comments
1.0	14 September 2018	SBH	Version 1, following reviews

### ROM SAF

The Radio Occultation Meteorology Satellite Application Facility (ROM SAF) is a decentralised processing centre under EUMETSAT which is responsible for operational processing of GRAS radio occultation data from the Metop satellites and RO data from other missions. The ROM SAF delivers bending angle, refractivity, temperature, pressure, and humidity profiles in near-real time and offline for NWP and climate users. The offline profiles are further processed into climate products consisting of gridded monthly zonal means of bending angle, refractivity, temperature, humidity, and geopotential heights together with error descriptions.

The ROM SAF also maintains the Radio Occultation Processing Package (ROPP) which contains software modules that will aid users wishing to process, quality-control and assimilate radio occultation data from any radio occultation mission into NWP and other models.

The ROM SAF Leading Entity is the Danish Meteorological Institute (DMI), with Cooperating Entities: i) European Centre for Medium-Range Weather Forecasts (ECMWF) in Reading, United Kingdom, ii) Institut D'Estudis Espacials de Catalunya (IEEC) in Barcelona, Spain, and iii) Met Office in Exeter, United Kingdom. To get access to our products or to read more about the project please go to: <http://www.romsaf.org>

### Intellectual Property Rights

All intellectual property rights of the ROM SAF products belong to EUMETSAT. The use of these products is granted to every interested user, free of charge. If you wish to use these products, EUMETSAT's copyright credit must be shown by displaying the words "copyright (year) EUMETSAT" on each of the products used.

## **Abstract**

ROPP-9.1 is a minor release of the ROM SAF's Radio Occultation Processing Package (ROPP). This report summarises some of the main science changes in ROPP 9.1. These include 1) modifications for GNOS processing, 2) improvements in the wave optics propagator and 3) changes to the L1/L2 bending angle forward models. Possible developments for future ROPP releases are discussed briefly.

## Contents

<b>1</b>	<b>Introduction</b>	<b>5</b>
<b>2</b>	<b>Updates for GNOS processing</b>	<b>6</b>
<b>3</b>	<b>Improvements to the wave optics propagator</b>	<b>8</b>
3.1	Changes to the computation of phase and amplitude at the LEO . . . . .	8
3.2	Treatment of the Earth's surface . . . . .	9
3.3	Modifications to the Full Spectrum Inversion . . . . .	10
<b>4</b>	<b>Modifications of L1/L2 bending angle modelling</b>	<b>12</b>
4.1	Electron density at the LEO satellite . . . . .	12
4.2	Removing bending above the LEO for a Chapman layer . . . . .	14
<b>5</b>	<b>Summary and future work</b>	<b>16</b>

## 1 Introduction

ROPP-9.1 is a minor release of the Radio Occultation Processing Package (Culverwell *et al.* 2015). The aim of this report is to summarise some of the science changes that are being incorporated into ROPP-9.1, and point to more detailed references – such as visiting scientist reports, and previous ROM SAF Reports (RSRs) – where possible.

The ROPP-9.1 science changes include:

1. Updates for processing GNOS measurements
2. Improvements in the wave optics simulation code
3. Improvements in the L1/L2 bending angle computations

The use of ROPP for GNOS processing is an important achievement for the ROM SAF, and the updates described here will enable ROPP-9.1 users to process GNOS data consistently with the current GNOS operational processing. The wave optics propagator changes are based on recent comparisons with another wave optics simulation code, which was more accurate in some difficult atmospheric cases, and user feedback from EUMETSAT. A modification to the Full Spectrum Inversion routine is also introduced. The L1/L2 changes address known approximations in the current modelling. These three changes are explained in more detail sections 2, 3 and 4. A summary and possible future work is briefly outlined in section 5.

## 2 Updates for GNOS processing

The gradual reduction of GNSS-RO observation numbers as a result of the decline of the COSMIC constellation means that it is important to fully exploit new sources of GNSS-RO data. Therefore, the new GNSS-RO data measured with the GNOS instrument on the Chinese FY3 satellites (Bia et al. 2014; Liao *et al.* 2016) is extremely important to the international community. The GNOS data from FY3-C is processed with ROPP preprocessing (ROPP-PP) routines, and this data is now assimilated operationally at both ECMWF and DWD. In addition, GNSS-RO data from FY3-D, launched in November 2017, is also likely to be available in 2018.

The use of ROPP-PP for operational GNOS processing is an important success for the ROM SAF developers. However, the GNOS processing required some specific modifications of the standard ROPP-PP routines. These modifications were originally developed and tested as part of a ROM SAF visiting scientist activity by Mi Liao at ECMWF (VS32). A detailed description of this visiting scientist work is contained in the report available at,

[http://www.romsaf.org/Publications/reports/romsaf\\_vs32\\_rep\\_v10.pdf](http://www.romsaf.org/Publications/reports/romsaf_vs32_rep_v10.pdf).

The modifications and prototype code developed during VS32, currently used for the operational processing of the FY3-C GNOS data, are currently in a local ROPP branch at the Chinese Meteorological Administration (CMA). These modifications have now been included in ROPP-9.1 in

```
SUBROUTINE ropp_pp_bending_angle_gnos.
```

The reasons for these modifications are discussed in VS32, but they will be reviewed here. Briefly, in the early work processing GNOS data with ROPP, it was found that around  $\sim 13\%$  of the refractivity profiles contained large biases, sometimes exceeding  $100\%$  near 20 km. These large biases were found to be mainly rising occultations which failed to produce an L2 bending angles below a 20 km straight line tangent altitude (SLTA). The standard ROPP-PP L2 phase extrapolation methods, followed by a wave optics retrieval, for L2 failed for GNOS because of this early loss of the L2, so an alternative approach was adopted. The new approach was based on the L1/L2 ionospheric bending angle modelling approaches given in RSR 17 available at,

[http://www.romsaf.org/general-documents/rsr/rsr\\_17.pdf](http://www.romsaf.org/general-documents/rsr/rsr_17.pdf)

which were developed primarily to investigate the direct assimilation of L1 and L2 bending angles. More specifically, the ionospheric bending,  $\alpha_i$ , at impact parameter  $a_j$ , assuming a one-dimensional “delta function” ionosphere is, can be approximated as (see RSR 17, section 3.1),

$$\alpha_i(a_j) = 2a_j \frac{k_4}{f_i^2} TEC \frac{r_0}{(r_0^2 - a_j^2)^{3/2}} \quad (2.1)$$

where the constant  $k_4 = 40.3 \text{ m}^3 \text{ s}^{-2}$ ,  $f_i$  is the signal frequency,  $TEC$  is the total electron content of the vertical profile, and  $r_0$  is the radius of the delta function. This is obviously a very simple approximation, but we only use it to provide an estimate of how the bending angle varies with height, in order to fit the L2 minus L1 bending angle differences. More specifically, the L2-L1 bending angle differences are approximated with,

$$\alpha_2(a_j) - \alpha_1(a_j) = 2a_j k_4 \left( \frac{1}{f_2^2} - \frac{1}{f_1^2} \right) TEC \frac{r_0}{(r_0^2 - a_j^2)^{3/2}}. \quad (2.2)$$

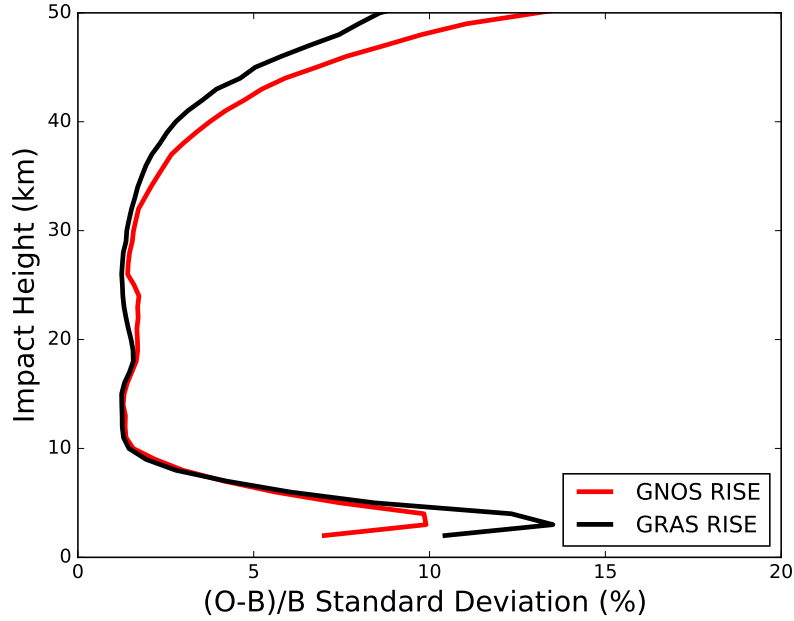


**Figure 2.1:** The standard deviation of the bending angle departure statistics for Metop-A GRAS (black line) and FY3-C GNOS (red line) rising measurements. The statistics are global and they are computed for the period April 3-30, 2018.

where  $f_1$  and  $f_2$  are the L1 and L2 frequency, respectively.

We assume that the peak electron density at  $r_0$  is 300 km above the surface, and estimate a fitting parameter,  $x$ , from a least-squares fit to the L2-L1 bending angle differences calculated in ROPP with the geometrical optics approach. This is achieved by minimising the cost function,

$$J(x) = \sum_j \left( \alpha_2(a_j) - \alpha_1(a_j) - x \frac{r_0}{(r_0^2 - a_j^2)^{3/2}} \right)^2 \quad (2.3)$$

with respect to  $x$ , where the sum is over L2-L1 bending angle differences for a set of impact parameters  $a_j$ , is usually taken over a 20 km vertical interval above the lowest L2 value. This 20 km fitting interval cannot go above 70 km. The parameter value that minimises the cost function,  $x_0$ , is then used to extrapolate the L2 bending angles,  $\alpha_2^e(a_k)$ , into the lower atmosphere,

$$\alpha_2^e(a_k) = \alpha_1(a_k) + x_0 \frac{r_0}{(r_0^2 - a_k^2)^{3/2}}. \quad (2.4)$$

and the L2 bending angles previously produced with the wave optics retrieval method are overwritten with the extrapolated values.

The approach also produces a noise estimate based on how well  $x_0$  fits the bending angle differences. Clearly, this method will result in vertical error correlations because of the extrapolation step. However, overall the GNOS bending angle departure statistics are comparable to other GNSS-RO instruments, and the data is suitable for operational assimilation at the NWP centres. For example, the globally averaged standard deviation of the for Metop-A GRAS and GNOS bending angle departure statistics for rising occultations, computed for 28 days in April 2018, are shown in Figure 2.1.

### 3 Improvements to the wave optics propagator

The ROPP-9 package included a new wave optics propagation tool, as described in RSR 28:

[http://www.romsaf.org/general-documents/rsr/rsr\\_28.pdf](http://www.romsaf.org/general-documents/rsr/rsr_28.pdf).

The ROPP-9 wave optics propagation tool is a standard implementation of the Multiple Phase Screen (MPS) approach (e.g., Karayel and Hinson, 1997; Sokolovskiy 2001). The ROPP code aims to be relatively simple, understandable, and adaptable. It is not as sophisticated or as general as the “WOP” wave optics code, developed by Michael Gorbunov (e.g., see Gorbunov, 2011), available via the EUMETSAT website), but the ROPP code will be developed further within the ROM SAF.

#### 3.1 Changes to the computation of phase and amplitude at the LEO

This change is discussed in more detail in RSR 28 (See RSR 28, section 3.2), and it relates to a change in the computation of the phase and amplitude at the LEO,  $\mathbf{U}(x_r, y_r)$ , given the phase and amplitude values at the final MPS screen,  $\mathbf{U}_f(y)$ . Briefly, this requires the solution of a diffraction integral (e.g, see Eq. 4, Gorbunov and Lauritsen, 2007),

$$\mathbf{U}(x_r, y_r) = \frac{1}{\sqrt{\lambda}} \int_y \mathbf{U}_f(y) \frac{\cos \phi}{\sqrt{r}} \exp(ikr - i\pi/4) dy \quad (3.1)$$

where the integration is performed over the entire final MPS screen,  $\lambda$  and  $k$  are the signal wavelength and wavenumber, respectively,  $r$  is the distance between a point on the final screen and the LEO position, and  $\cos \phi$  is the obliquity factor (e.g., see Goodman, 1996, section 3.1). This is computed in SUBROUTINE `ropp_pp_wopt_propagate_to_leo`. ROPP-9 uses the standard Fresnel approximation in the exponent of the diffraction integral (see Goodman, 1996, section 4.2), and then evaluates this integral efficiently by summing Fresnel functions. However, recent detailed comparisons with simulations provided by Joel Rasch (Molflow, Sweden) indicated that this approximation can lead to errors in the lowest 2 km, when the bending angles are large. A relatively simple code change has been tested and implemented in ROPP-9.1, that improves the bending angle computation. An example of the improvement from RSR 28 is shown in Figure 3.1, for a “difficult case”<sup>1</sup> with a large bending angle gradient caused by a sharp refractive index gradient across a temperature inversion. These bending profiles have been smoothed with a Gaussian smoother, and the final MPS screen is split into 32 m vertical intervals for computing the diffraction integral (Eq. 3.1). In this case, the ROPP-9 implementation of the diffraction integral had the correct shape, but it was failing to reproduce the large bending angles exceeding 0.05 radians. Clearly, the ROPP-9.1 modification, described in RSR 28, is considerably better.

As noted above, the results shown in Figure 3.1 are based on splitting the final MPS screen into 32 m intervals (`nsample = 32`) when computing the diffraction integral, and this sampling appears to be necessary for computing very sharp bending angle features. We therefore currently recommend the following configuration file for wave optics computations:

<sup>1</sup>A set of 55 one-dimensional atmospheric profiles are available from the ROM SAF pages for use with the wave optics code. We present “case 12” here which is “difficult” because the maximum refractivity gradients almost at the ducting level.

```

! =====
! Namelist of ROPP wave optics propagator configuration parameters
! =====

&config_wopt

! -----
! Grid specifications
! -----

nx = 401,                ! No. of horizontal screens (must be odd)

log2ny = 19,            ! log2 of number of vertical points in each screen

n_leo = 20000,          ! Number of points (and times) for
                        ! which phases will be calculated

nsample = 32,           ! Number of points in each 'sample' of the final screen,
                        ! used when calculating signal at LEO

dx = 5.0e3,             ! Separation of screens (m)

dy = 1.0,               ! Separation of vertical points (m)

ymin = -3.0e5,          ! Lower limit of screens (m)

y_apodize = 1.2e5,      ! Height where apodization starts (m)

leo_altitude = 8.0e5,   ! LEO altitude (m)

gps_altitude = 2.02e7,  ! GNSS altitude (m)

tpt_altitude = 8.0e4,   ! Nominal TPT altitude (m)

delta_t = 0.005,        ! Time between phase/amp samples (s)

! -----
! Mandatory end of namelist delimiter
! -----

/

```

### 3.2 Treatment of the Earth's surface

The second wave optics modification deals with the treatment of the Earth's surface, and it is based on feedback on ROPP-9 from Riccardo Notarpietro (EUMETSAT). The ROPP wave optics code does not include reflections at the Earth's surface. Similar to Sokolovskiy (2001) we have a "soft boundary" and damp the signal close to and below the surface, in order to reduce an unphysical diffraction

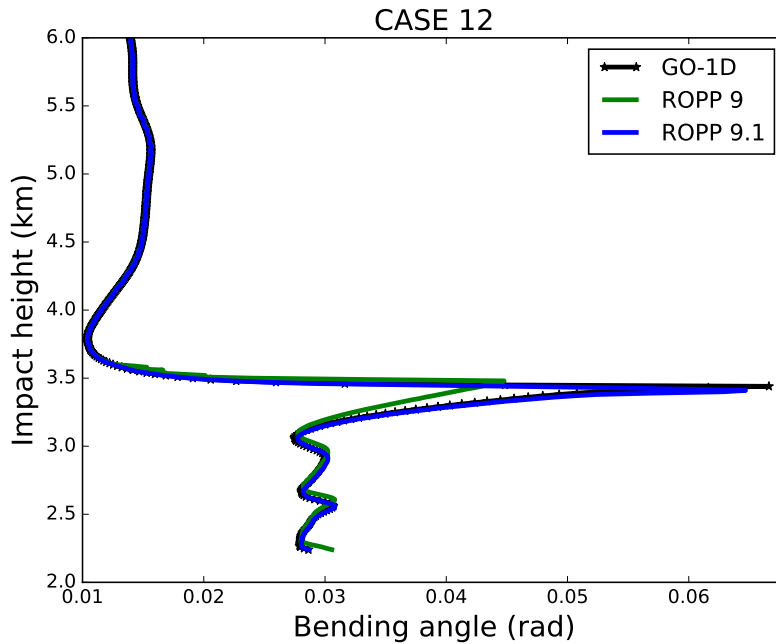


**Figure 3.1:** The retrieved bending angles produced with the wave optics propagator and FSI inverse for ROPP 9 (green line), ROPP 9.1 (blue line) and the one-dimensional geometrical optics simulation (black line). See RSR 28 for more details about this ROPP-9.1 change and for a definition of “case 12”.

pattern caused by treating the boundary as a sharp edge. This is also called a “window function”, and it is computed in SUBROUTINE `ropp_pp_wopt_window`.

In ROPP-9 we damp the complex signal,  $\mathbf{U}$ , below 1 km above the Earth’s surface using a Gaussian function of the form

$$\mathbf{U} \rightarrow \mathbf{U} \times \exp\left(-\left(\frac{y-y_b}{W}\right)^2\right) \quad (3.2)$$

where  $y$  is the height above the surface at the MPS screen,  $y_b$  is 1 km above the surface, and  $W$  is set to 1 km. The values of  $y_b$  and  $W$  do not appear to be uniquely defined by any obvious theory, and we selected them based on the reduction of the unphysical diffraction effects noted above. However, we may have applied too much damping, resulting in an early truncation of the bending angle profile in some cases. Specifically, Riccardo Notarpietro (EUMETSAT) reported that the ROPP-9 implementation appeared to smooth too much near the boundary when compared with Michael Gorbunov’s “WOP code”, and he tested various alternative values. As a result, the ROPP parameters have been revised for ROPP-9.1 such that the damping is now only applied below the surface ( $y_b = 0$  km) and the width,  $W$ , has been reduced from 1 km to 500 m. However, we emphasise that users may wish to continue to experiment with the values of these parameters, and more feedback would be welcomed.

### 3.3 Modifications to the Full Spectrum Inversion

We have made a small modification to SUBROUTINE `ropp_pp_wopt_fsi_quick`. This simplified Full Spectrum Inversion (FSI) routine (Jensen *et al.*, 2003) is useful for checking that the wave optics output produces accurate bending angles. Fundamentally, this routine is a Fast Fourier Transform (FFT) of interpolated phase ( $\phi(t)$ ) and amplitude ( $A(t)$ ) values at the LEO satellite. Before computing

the FFT, the interpolated signal at the LEO is multiplied by a phase model,

$$U(t) = A(t) \exp(i(\phi(t) - D_m t)) \quad (3.3)$$

where in this simple FSI implementation  $D_m$  is given by the minimum value of the excess Doppler at the LEO. In ROPP-9.1, we now stop the search for the minimum excess Doppler once the signal amplitude has fallen below 1 % of the maximum value, otherwise we can obtain erroneous Doppler values when the amplitude is very low, with the FSI failing to produce any bending angles in some cases.

## 4 Modifications of L1/L2 bending angle modelling

ROPP-9.1 includes two modifications aimed at potentially improving single frequency processing. The first modification introduces a new L1/L2 bending angle term to partially correct for assuming that the electron density is unity at the LEO, when retrieving bending angles from the Doppler values. The second change removes the bending associated with the section of ray-path from above the LEO to infinity, which is currently included in the “Zorro function” computation given in RSR 17 (see the link to RSR 17, given in Section 2). These modifications both reduce the magnitude of forward modelled bending angle values.

### 4.1 Electron density at the LEO satellite

It is well known that the bending angles are retrieved from the Doppler shift values assuming that the refractive index at both satellites is unity. This assumption is reasonable for the GPS satellite, where the electron density will be low, but it is not valid for a LEO satellite at an altitude of typically 800 km or below. Fortunately, for circular orbits this error cancels out in the standard ionospheric correction of dual frequency measurements, as shown by Schreiner *et al.* (Appendix A, 1999). In this case the impact parameter derived from the Doppler shift is correct, and the error caused by the electron density only affects the retrieved bending angles. However, this bending angle error scales as  $1/f_i^2$ , where  $f_i$  is the frequency of the signal, and it cancels out in the standard dual frequency ionospheric correction. Clearly, this cancellation does not occur for the L1 and L2 bending angles individually, so we introduce a correction term. The frequency scaling for circular orbits can be shown as follows. Consider the impact parameter value at the LEO satellite,  $a$ , for a signal with frequency  $f_i$ ,

$$a = n_l^i r_l \sin \phi_l \quad (4.1)$$

where  $r_l$  is the radius of the LEO,  $\phi_l$  is the angle between the ray-path and the local radius vector at the LEO, and  $n_l^i$  is the refractive index at the LEO satellite. The latter can be written as  $n_l^i = 1 - k_4 n_e(r_l) / f_i^2$ , where  $n_e(r_l)$  is the electron density at the LEO. Assuming that the impact parameter is unchanged as a result of mis-specifying the refractive index at the LEO, we can write

$$\delta a = \delta n_l^i r_l \sin \phi_l + n_l^i r_l \cos \phi_l \delta \phi_l = 0 \quad (4.2)$$

where, since we assume the refractive index is unity at the LEO the refractive index error,  $\delta n_l^i$ , is given by,

$$\begin{aligned} \delta n_l^i &= 1 - \left( 1 - \frac{k_4}{f_i^2} n_e(r_l) \right) \\ &= \frac{k_4}{f_i^2} n_e(r_l) \end{aligned} \quad (4.3)$$

Rearranging Eq.4.2 gives,

$$\begin{aligned} \delta \phi_l &= - \frac{k_4}{f_i^2} \frac{\sin \phi_l}{\cos \phi_l} n_e(r_l) \\ &\simeq - \frac{k_4}{f_i^2} \frac{a}{\sqrt{r_l^2 - a^2}} n_e(r_l). \end{aligned} \quad (4.4)$$

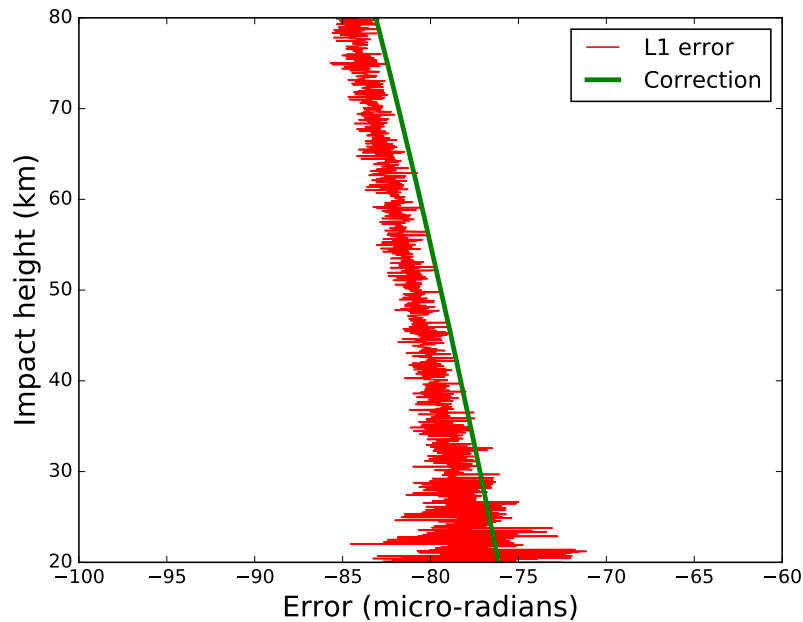


**Figure 4.1:** The error in the retrieved L1 bending angles for a CHAMP occultation (red line) and the correction given by Eq. 4.4.

Therefore, the L1 and L2 bending angles will be biased low. Figure 4.1 shows an extreme example for a 1D simulation using a CHAMP orbit for an L1 signal, as used by Marquardt and Healy (2005). In the simulation, the electron density is assumed to be a Chapman layer with a peak electron density of  $n_m = 3 \times 10^{12} \text{m}^{-3}$ , peaking at an altitude of 300 km, and with a width,  $H = 60$  km. The L1 bending angles values are typically around 300 micro-radians in the stratosphere for this ionosphere. The bending angles are computed both directly by evaluating the change in direction of the ray vector at the ends of the ray-path, and via the Doppler shift assuming the refractive index at the receiver is unity, as with the actual measurements. The CHAMP satellite was at an altitude of about 420 km, so it is much closer to the peak electron density than the COSMIC or Metop satellites. This low altitude produces extremely large L1 bending angle errors (red line) of around -80 micro-radians. This error is derived by comparing the bending angles computed from the Doppler shift, with those computed from the change in ray direction. For context, note that typically we assume an uncertainty of 3 micro-radians when assimilating corrected bending angles into NWP systems, so they errors in Figure 4.1 are much larger than would be expected for corrected bending angles. The errors in the L1 bending angle profile is well modelled with the new correction term. The “residual” errors caused by  $n_e(r_I)$  remaining after this correction are probably related to the non-circular component of the CHAMP orbits.

It may be possible to improve this correction in the future to account for the non-circular satellite orbits, and recently Syndergaard and Kirchengast (2018, unpublished) have derived an expression for this error term. However, this potential improvement will require passing additional satellite velocity information to the bending angle forward model.

## 4.2 Removing bending above the LEO for a Chapman layer

This work is based on the approach for calculating the ray bending for a truncated Chapman layer, given in Appendix A.4 in RSR 17,

[http://www.romsaf.org/general-documents/rsr/rsr\\_17.pdf](http://www.romsaf.org/general-documents/rsr/rsr_17.pdf).

However, it is useful to review the derivation here for clarity.

The ionospheric bending angle,  $\alpha_i$ , as a function of impact parameter,  $a$ , for a one-dimensional electron density profile,  $n_e(r)$ , can be approximated with,

$$\alpha_i(a) = \frac{2ak_4}{f_i^2} \int_a^\infty \frac{dn_e(r)}{\sqrt{r^2 - a^2}} dr \quad (4.5)$$

where  $r$  is the radius value and  $f_i$  is the frequency of the signal. The ‘‘Zorro’’ function defined in RSR 17 provides an approximate solution to this integral for a Chapman layer ionosphere. The Chapman layer is defined as,

$$n_e(r) = n_m \exp\left(\frac{1}{2}(1 - u - \exp(-u))\right) \quad (4.6)$$

where  $u = (r - r_o)/H$ ,  $n_m$  is the peak electron density,  $r_o$  is the radius value at the peak electron density, and  $H$  determines the width of the Chapman layer. The radial gradient of the electron density is then,

$$\frac{dn_e(r)}{dr} = \frac{n_m \sqrt{e}}{2H} \left( \exp\left(-\frac{3}{2}u\right) - \exp\left(-\frac{1}{2}u\right) \right) \exp\left(-\frac{1}{2}\exp(-u)\right) \quad (4.7)$$

Approximating  $r + a \simeq r_o + a$  and inserting Eq. 4.7 in Eq. 4.5 gives,

$$\alpha_i(a) \simeq \frac{ak_4 \sqrt{en_m}}{H f_i^2 \sqrt{r_o + a}} \int_a^\infty \frac{(\exp(-\frac{3}{2}u) - \exp(-\frac{1}{2}u)) \exp(-\frac{1}{2}\exp(-u))}{\sqrt{r - a}} dr \quad (4.8)$$

The Zorro function computes this integral with a Padé approximation, noting that the integral is only a function of the combined parameter  $(r_o - a)/H$ . The upper limit of Eq. 4.8 is infinity, and the assumption is that both the LEO and GPS satellites are at a large radius, where the electron density is effectively zero. This may be a reasonable assumption for the GPS satellite, but it is not valid for the LEO at an altitude of around 800 km or below. However, we can estimate the bending above the LEO assuming the Chapman layer,  $\Delta\alpha_i(r_l)$ , and then subtract it from the bending angle produced with the Zorro function. The bending above the LEO can be written as,

$$\Delta\alpha_i(r_l) \simeq \frac{1}{2} \frac{ak_4 \sqrt{en_m}}{H f_i^2 \sqrt{r_o + a}} \int_{r_l}^\infty \frac{(\exp(-\frac{3}{2}u) - \exp(-\frac{1}{2}u)) \exp(-\frac{1}{2}\exp(-u))}{\sqrt{r - a}} dr \quad (4.9)$$

where the lower limit of the integral is now  $r_l$ , and the introduction of a factor of 1/2 is because we are only dealing with a correction to one half of the ray-path, on the side from the tangent point to the receiver. As shown in RSR 17 (Sections A.2 and A.4), this integral can be evaluated by a term-by-term integration of a series expansion, and the expansion converges reasonably rapidly if the the LEO is above the peak of the Chapman layer ( $r_l \geq r_o$ ). We reproduce the main steps of the solution given in RSR 17 here for clarity. We can re-write,

$$\begin{aligned} u &= \frac{r - r_o}{H} \\ &= \frac{r - r_l}{H} - \frac{r_o - r_l}{H} \end{aligned} \quad (4.10)$$

and define,

$$\begin{aligned} w &= \frac{r - r_l}{H} \\ \beta &= \exp\left(\frac{r_o - r_l}{H}\right) \end{aligned} \quad (4.11)$$

Then

$$\begin{aligned} & \int_{r_l}^{\infty} \frac{(\exp(-\frac{3}{2}u) - \exp(-\frac{1}{2}u)) \exp(-\frac{1}{2} \exp(-u))}{\sqrt{r-a}} dr \\ &= \int_0^{\infty} \frac{(\beta^{3/2} \exp(-\frac{3}{2}w) - \beta^{1/2} \exp(-\frac{1}{2}w)) \exp(-\frac{\beta}{2} \exp(-w))}{\sqrt{Hw + r_l - a}} H dw \\ &= \sqrt{H\beta} \int_0^{\infty} \frac{(\beta \exp(-\frac{3}{2}w) - \exp(-\frac{1}{2}w)) \exp(-\frac{\beta}{2} \exp(-w))}{\sqrt{w+c}} dw \end{aligned} \quad (4.12)$$

where  $c = (r_l - a)/H$ . The super-exponential is expanded,

$$\exp\left(-\frac{\beta}{2} \exp(-w)\right) \simeq 1 - \frac{\beta}{2} \exp(-w) + \left(\frac{\beta}{2}\right)^2 \frac{\exp(-2w)}{2!} + \dots + \frac{(-1)^n}{n!} \left(\frac{\beta}{2}\right)^n \exp(-nw) \quad (4.13)$$

and this expansion is used in Eq. 4.12. This leads to a summation of standard integrals of the form,

$$\int_0^{\infty} \frac{\exp(-kw)}{\sqrt{w+c}} dw = \sqrt{\frac{\pi}{k}} \exp(kc) \operatorname{erfc}(\sqrt{kc}). \quad (4.14)$$

We find,

$$\begin{aligned} & \sqrt{H\beta} \int_0^{\infty} \frac{(\beta \exp(-\frac{3}{2}w) - \exp(-\frac{1}{2}w)) \exp(-\frac{\beta}{2} \exp(-w))}{\sqrt{w+c}} dw \\ &= \sqrt{H\beta\pi} \sum_{n=0}^{\infty} \frac{(-1)^n}{n!} \left(\frac{\beta}{2}\right)^n \left( \frac{\beta u_{n+3/2}}{\sqrt{n+3/2}} - \frac{u_{n+1/2}}{\sqrt{n+1/2}} \right) \end{aligned} \quad (4.15)$$

where for  $(m = 1, 3)$ ,

$$u_{n+m/2} = \exp((n+m/2)c) \operatorname{erfc}(\sqrt{(n+m/2)c}). \quad (4.16)$$

The summation in Eq. 4.15 can be simplified to give

$$2\sqrt{H\beta\pi} \sum_{n=0}^{\infty} \frac{(-1)^{n+1} \sqrt{n+1/2}}{n!} \left(\frac{\beta}{2}\right)^n u_{n+1/2}. \quad (4.17)$$

If we substitute the summation Eq. 4.17 into the integral in Eq. 4.9 we obtain an estimate for the bending above the LEO for a Chapman layer,

$$\Delta\alpha_i(r_l) \simeq \frac{k_4 a n_m \sqrt{e\pi\beta}}{f_i^2 \sqrt{H(r_o+a)}} \sum_{n=0}^{\infty} \frac{(-1)^{n+1} \sqrt{n+1/2}}{n!} \left(\frac{\beta}{2}\right)^n u_{n+1/2}. \quad (4.18)$$

This term can then be subtracted from the ionospheric bending computed with the Zorro function. ROPP-9.1 includes SUBROUTINE `ropp_fm_iono_bangle_above_leo`, and the associated tangent-linear and adjoint routines, to compute this summation.

## 5 Summary and future work

Some of the main science changes in ROPP-9.1 have been reviewed. The GNOS changes will enable ROPP users to process GNOS data consistently with the current operational processing of this data. Clearly, if ROPP-PP is developed further for GNOS processing – or in fact any other GNSS-RO missions – then the aim will be to update future ROPP releases accordingly. The wave optics propagator changes are quite minor in terms of code changes, but they have a clear impact on the quality of the simulated bending angle profiles. One generalisation of the wave optics propagator that will be introduced in the future will be use of two-dimensional (2D) refractivity planar sections in the simulation, rather than one-dimensional refractivity profiles. Prototype code for this change is currently being tested at ECMWF. One advantage of these 2D simulations is that it will enable the investigation of horizontal gradient errors. The changes in the L1/L2 bending angle forward models mean that they should be more consistent with the actual measurement geometry, and the assumptions made in the processing of the measurements. These changes may be important for single frequency processing of GPS/MET for example, but this will have to be demonstrated in the future. To date, a Chapman layer has been assumed in both the Zorro function and the correction presented here, but we may have to consider a numerical approach in the future if alternative ionospheric profiles are assumed.

### Acknowledgments

Many thanks to Ian Culverwell (ROM SAF, UK Met Office) for checking the algebra in section 4.2. Thanks also to Joel Rasch (Molflow, Sweden) for access to his wave optics propagator simulations that led to the wave optics propagator improvements in ROPP-9.1.

## References

- Bai, W. H., Y. Q. Sun, Q. F. Du, G. L. Yang, Z. D. Yang, P. Zhang, Y. M. Bi, X. Y. Wang, C. Cheng, and Y. Han, 2014: An introduction to the FY3 GNOS instrument and mountain-top tests. *Atmos. Meas. Tech.*, **7**, 1817–1823.
- Culverwell, I. D., H. W. Lewis, D. Offiler, C. Marquardt, and C. P. Burrows, 2015: The radio occultation processing package, ROPP. *Atmos. Meas. Tech.*, **8**, 1887–1899, doi:10.5194/amt-8-1887-2015.
- Goodman, J. W., 1996: *Introduction to Fourier Optics*. McGraw-Hill, International Editions.
- Gorbunov, M. E., 2011: Wave optics propagator package: Description and user guide. Tech. Rep. Tech. Report for contract EUM/co/10/460000812/CJA order 4500005632, EUMETSAT, Darmstadt, Germany.
- Gorbunov, M. E., and K. B. Lauritsen, 2007: Linearized Zverev Transform and its application for modeling radio occultations. *Radio Sci.*, **42**, RS3023, doi:10.1029/2006RS003590.
- Jensen, A., M. Lohmann, H.-H. Benzon, and A. Nielsen, 2003: Full Spectrum Inversion of radio occultation signals. *Radio Sci.*, **38**, 1040, doi:10.1029/2002RS002763.
- Karayel, E., and D. Hinson, 1997: Sub-Fresnel-scale vertical resolution in atmospheric profiles from radio occultation. *Radio Sci.*, **32**, 411–423.
- Liao, M., P. Zhang, G.-L. Yang, Y.-M. Bi, Y. Liu, W.-H. Bai, X.-G. Meng, Q.-F. Du, and Y.-Q. Sun, 2016: Preliminary validation of the refractivity from the new radio occultation sounder GNOS/FY-3C. *Atmos. Meas. Tech.*, **9**, 781–792,.
- Marquardt, C., and S. B. Healy, 2005: Measurement noise and stratospheric gravity wave characteristics obtained from gps occultation data. *Journal of the Meteorological Society of Japan. Ser. II*, **83**, 3, 417–428.
- Schreiner, W. S., S. V. Sokolovskiy, C. Rocken, and D. C. Hunt, 1999: Analysis and validation of GPS/MET radio occultation data in the ionosphere. *Radio Sci.*, **34**, 949–966.
- Sokolovskiy, S. V., 2001: Modeling and inverting radio occultation signals in the moist troposphere. *Radio Sci.*, **36**, 441–458.

**ROM SAF (and earlier GRAS SAF) Reports**

SAF/GRAS/METO/REP/GSR/001	Mono-dimensional thinning for GPS Radio Occultation
SAF/GRAS/METO/REP/GSR/002	Geodesy calculations in ROPP
SAF/GRAS/METO/REP/GSR/003	ROPP minimiser - minROPP
SAF/GRAS/METO/REP/GSR/004	Error function calculation in ROPP
SAF/GRAS/METO/REP/GSR/005	Refractivity calculations in ROPP
SAF/GRAS/METO/REP/GSR/006	Levenberg-Marquardt minimisation in ROPP
SAF/GRAS/METO/REP/GSR/007	Abel integral calculations in ROPP
SAF/GRAS/METO/REP/GSR/008	ROPP thinner algorithm
SAF/GRAS/METO/REP/GSR/009	Refractivity coefficients used in the assimilation of GPS radio occultation measurements
SAF/GRAS/METO/REP/GSR/010	Latitudinal Binning and Area-Weighted Averaging of Irregularly Distributed Radio Occultation Data
SAF/GRAS/METO/REP/GSR/011	ROPP 1dVar validation
SAF/GRAS/METO/REP/GSR/012	Assimilation of Global Positioning System Radio Occultation Data in the ECMWF ERA-Interim Re-analysis
SAF/GRAS/METO/REP/GSR/013	ROPP PP validation
SAF/ROM/METO/REP/RSR/014	A review of the geodesy calculations in ROPP
SAF/ROM/METO/REP/RSR/015	Improvements to the ROPP refractivity and bending angle operators
SAF/ROM/METO/REP/RSR/016	Simplifying EGM96 undulation calculations in ROPP
SAF/ROM/METO/REP/RSR/017	Simulation of L1 and L2 bending angles with a model ionosphere
SAF/ROM/METO/REP/RSR/018	Single Frequency Radio Occultation Retrievals: Impact on Numerical Weather Prediction
SAF/ROM/METO/REP/RSR/019	Implementation of the ROPP two-dimensional bending angle observation operator in an NWP system
SAF/ROM/METO/REP/RSR/020	Interpolation artefact in ECMWF monthly standard deviation plots
SAF/ROM/METO/REP/RSR/021	5th ROM SAF User Workshop on Applications of GPS radio occultation measurements
SAF/ROM/METO/REP/RSR/022	The use of the GPS radio occultation reflection flag for NWP applications
SAF/ROM/METO/REP/RSR/023	Assessment of a potential reflection flag product
SAF/ROM/METO/REP/RSR/024	The calculation of planetary boundary layer heights in ROPP
SAF/ROM/METO/REP/RSR/025	Survey on user requirements for potential ionospheric products from EPS-SG radio occultation measurements

**ROM SAF (and earlier GRAS SAF) Reports (cont.)**

SAF/ROM/METO/REP/RSR/026	Estimates of GNSS radio occultation bending angle and refractivity error statistics
SAF/ROM/METO/REP/RSR/027	Recent forecast impact experiments with GPS radio occultation measurements
SAF/ROM/METO/REP/RSR/028	Description of wave optics modelling in ROPP-9 and suggested improvements for ROPP-9.1
SAF/ROM/METO/REP/RSR/029	Testing reprocessed GPS radio occultation datasets in a reanalysis system
SAF/ROM/METO/REP/RSR/030	A first look at the feasibility of assimilating single and dual frequency bending angles
SAF/ROM/METO/REP/RSR/031	Sensitivity of some RO measurements to the shape of the ionospheric electron density profile
SAF/ROM/METO/REP/RSR/032	An initial assessment of the quality of RO data from KOMPSAT-5

ROM SAF Reports are accessible via the ROM SAF website: <http://www.romsaf.org>